Optical resonances in the scattering of light from a nanostructured metal surface: A three-dimensional numerical study

T. V. Teperik[1,2,*] and A. G. Borisov[2,3]

[1]*Laboratoire Charles Fabry de l'Institut d'Optique, CNRS, Université Paris-Sud, Campus Polytechnique, RD 128, 91127 Palaiseau Cedex, France*

[2]*Donostia International Physics Center (DIPC), P. Manuel de Lardizabal 4, San Sebastián 20018, Spain*

[3]*Laboratoire des Collisions Atomiques et Moléculaires, UMR CNRS-Université Paris-Sud 8625, Bât. 351, Université Paris-Sud, 91405 Orsay Cedex, France*

(Received 5 March 2009; revised manuscript received 28 April 2009; published 8 June 2009)

We present the full three-dimensional numerical study of the scattering of light by the gold substrate composed of square periodic array of inverted pyramidal pits. The time-dependent wave-packet-propagation approach was used to extract the complete scattering matrix as well as the near fields. The role of the pit-localized and surface-supported plasmonic modes in resonant reflection spectra and field enhancement is revealed. We show that the resonances in the specular reflection arise because of the excitation of the pit-localized plasmons while resonant absorption is linked with excitation of the surface-plasmon polaritons. For certain structure parameters absorption can reach 100%. Our theoretical results are in a good agreement with recently published experimental data [N. M. B. Perney *et al.*, Opt. Express **14**, 847 (2006); Phys. Rev. B **76**, 035426 (2007)]. We also show that present structure allows one to obtain zero specular reflection where all scattered intensity is redirected into the grazing beams.

DOI: 10.1103/PhysRevB.79.245409 PACS number(s): 73.20.Mf, 78.20.Bh, 61.46.−w

I. INTRODUCTION

Interaction of light with periodically nanostructured metal surfaces has been a subject of numerous experimental and theoretical studies over the past years.[1–3] The large plethora of resonant phenomena has been revealed and discussed such as extraordinary transmission through the subwavelength hole arrays[4–11] and metallic grating,[5,12–15] absorption of the incoming radiation,[16–20] and coherent thermal emission.[21–23] The resonances represent sharp features in the frequency dependence of the scattering matrix. From the time dependent point of view, they reflect the existence of the long-lived (slowly decaying) electromagnetic near-field modes "trapped" by the structure. The surface-plasmon polaritons (SPPs) have been shown to play an essential role in above phenomena providing an efficient intermediate state that couples incident, diffracted, and transmitted lights.[5,11,24] Along with periodic substrates, launching and guiding of SPPs on specially designed surfaces are currently the subject of intense research.[1,25–29]

In a number of recent studies, on the example of spherical voids, it has been demonstrated that the substrates possessing periodic arrays of voids buried beneath the planar surface of metal constitute a new class of plasmonic nanostructures showing two types of the optical resonances.[30–32] Both the delocalized SPPs and void localized plasmons (LPs) are hosted by these nanostructures and can be resonantly excited with incoming light.[30,33–35] The void LPs are screened by the surrounding metal and thus basically do not interact with each other. As a result, the trapped-electromagnetic-field modes associated with void LPs show flat frequency dispersion with two-dimensional (2D) wave vector in the surface plane. This is quite a peculiar property which strongly differs the above structure from, e.g., planar metallic plasmonic crystals with periodic arrangement of metallic nano-objects.[36–40] In the latter case, the plasmons localized at individual nano-objects interact through the near and radiative fields so that the plasmonic bands are strongly dispersive.

The energy of the void localized plasmons, as well as their coupling to the incident light, depends on the geometry and dielectric filling of voids. Together with flat dispersion curves these properties allow one to achieve the total omnidirectional absorption of the incident light.[41,42] Moreover, while most of the surface-enhanced Raman-scattering (SERS) studies[43] rely on the plasmonic enhancement effects due to the uncontrollable roughness, periodic structures with voids offer a possibility to create tunable substrates for the reproducible SERS.[31,44–46] Indeed, similar to the nanoparticles and nanoparticle assemblies,[47–51] excitation of the void LPs is associated with strong enhancement of the near fields.

The obvious technical challenge in the experimental realization of periodic void arrays invites for the theoretical effort in both (i) qualitative prediction of the major characteristics of the LPs and their coupling to incoming light and SPPs and (ii) providing quantitative information on the frequencies of the LPs, associated near fields, as well as on the scattering properties of the nanostructured surfaces. The latter allows one to connect between the resonant structures in experimental reflection spectra and the underlying trapped electromagnetic modes, including the LPs.

Following the in-depth studies on the periodic arrays of metal substrates with spherical voids,[30–35,41,42] the gold substrates composed of arrays of inverted pyramidal pits have recently been fabricated and their reflection spectra have been measured.[45,46] Based on the simple model it has been argued that the dips in the reflectivity spectra can be attributed to the excitation of the localized plasmons confined at the pit sidewalls.[45] However, no parameter-free study has been performed to support the above idea. Present work closes this gap.

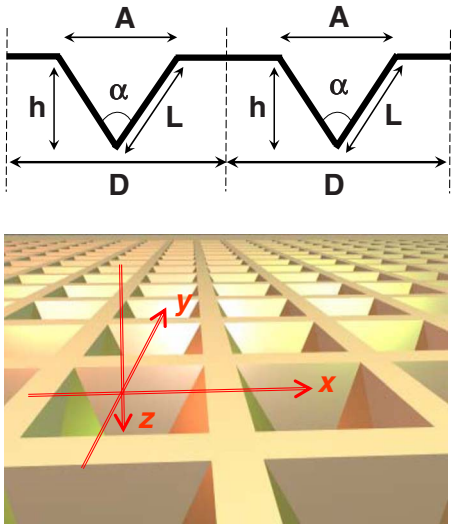

FIG. 1. (Color online) Schematic representation of the surface with square array of the inverted square pyramidal pits. Upper panel shows the cross section of the array by the (xz) plane perpendicular to the surface and containing the apex of the pit. D is the period of the structure, A is the pit aperture, h is the pit depth, and α is a pit apex angle. Lower panel defines the coordinate frame. The radiation is incident along the normal to the surface (the z direction).

We report on the full three-dimensional (3D) numerical study of the scattering of light by the gold substrate composed of square periodic array of inverted pyramidal pits. Normal incidence geometry is considered. Far fields (scattering matrix) and near fields are calculated with time-domain wave-packet propagation (WPP) approach.[52] The theoretical results are in good agreement with experimental data for the wide range of the nanostructure parameters. This allows us to unravel the role of pit localized plasmons and delocalized SPPs in the experimentally measured reflectivity spectra. We demonstrate that in the present system the excitation of the LPs reveals itself in the enhanced specular reflection and not in the enhanced absorption of the incoming light as has been proposed earlier.[45,46] We find that besides excitation of trapped modes localized at the sidewalls of the pyramidal pits, the present system shows a number of interesting features. Among them are polarization-independent 100% resonant absorption at normal incidence and suppression of specular reflection where all scattered intensity is in the diffracted beams.

The paper is organized as follows. Section II introduces the system under the study and presents a brief outline of the theoretical method. Section III is devoted to the results and their discussion. Finally, conclusions (Sec. IV) close the paper.

II. METHODS

The system under the study is sketched in Fig. 1. It is equivalent to the one studied experimentally in Refs. 45 and 46. The nanostructured gold surface consists of the square array of the inverted pyramidal pits. D is the period of the array along x and y in-plane directions. The z axis is perpendicular to the structure with surface located at $z=0$. The geometry of the pyramidal pit is given by the aperture A and the apex pit angle α. For all studied arrays we have used $\alpha=70.5°$ consistent with experimentally studied samples. The pit depth h is then readily obtained as $h=A\cot(\alpha/2)/2$. In order to reveal the role of plasmon modes in optical reflection spectra, the calculations have been performed for the arrays with different combination of D and A parameters. The normal incidence has been considered with the light incident along the z axis and polarized in such a way that the electric-field vector $\mathbf{E}$ is along the x axis.

Absorption and reflection properties of the nanostructured surface are calculated by means of the WPP method. It is based on the representation of Maxwell's equations in the form of the Schrödinger equation for which the initial value problem is numerically solved by a time-stepping algorithm. A detailed description can be found elsewhere.[52,53] Here we give only the details specific for the present study.

The metal is described by the complex dielectric function ϵ defined within the Drude model:

$$\epsilon(\omega)=1-[\omega_p^2/(\omega^2+i\omega\gamma)],$$

where $\omega_p=7.9$ eV is the bulk-plasmon frequency and $\gamma=0.09$ eV is the attenuation of gold.[54] In order to represent Maxwell's equations in the form of the Schrödinger equation we proceed as follows. Let $\mathbf{D}=\mathbf{E}+\mathbf{P}$, where $\mathbf{D}$, $\mathbf{E}$, and $\mathbf{P}$ are, respectively, the electric induction, the electric field, and the medium polarization vector. In the Drude model, the medium-polarization vector evolves in time according to

$$\partial^2\mathbf{P}/\partial t^2+\gamma\,\partial\mathbf{P}/\partial t=\omega_p^2\mathbf{E}. \tag{1}$$

Equation (1) must be solved with zero initial conditions, $\mathbf{P}=\partial\mathbf{P}/\partial t=0$ at $t=0$. With an auxiliary field $\mathbf{Q}$ defined by $\partial\mathbf{P}/\partial t=\omega_p\mathbf{Q}$, Maxwell's equations take the Schrödinger form

$$i\,\partial\Psi/\partial t=H\Psi, \tag{2}$$

where the wave function Ψ and the Hamiltonian H are

$$\Psi=\begin{pmatrix}\mathbf{E}\\ \mathbf{B}\\ \mathbf{Q}\end{pmatrix}, \tag{3}$$

$$H=H_0+V=\begin{pmatrix}0 & ic\,\nabla\times & -i\omega_p\\ -ic\,\nabla\times & 0 & 0\\ i\omega_p & 0 & 0\end{pmatrix}+\begin{pmatrix}-i\sigma & 0 & 0\\ 0 & 0 & 0\\ 0 & 0 & -i\gamma\end{pmatrix}. \tag{4}$$

H_0 is the Hermitian part of the Hamiltonian and V is non-Hermitian part. The quantities ω_p and γ are position dependent so that $\omega_p=0$ and $\gamma=0$ everywhere outside the metal. An absorbing layer with position-dependent conductivity $\sigma(z)$ is introduced above the surface close to the grid boundary in order to suppress artificial reflections of the wave packet.[55,56] When the attenuation inside the metal and absorbing layer are absent, $H=H_0$, and the norm of the wave function $\|\Psi\|^2=\int d\mathbf{r}\Psi^\dagger\Psi$ is conserved due to course of time

propagation. The norm here is proportional to the total electromagnetic energy of the wave packet.[53]

Provided initial conditions $\Psi(t=0)\equiv\Psi_0$, solution of Eq. (2) is obtained via the short-time propagation with split-operator technique[57,58]

$$\Psi(t+\Delta t)=e^{-i(\Delta t/2)V}e^{-i\Delta t H_0}e^{-i(\Delta t/2)V}\Psi(t), \tag{5}$$

where the time step Δt typically equals 0.01 fs. With wave-function representation on the 3D spatial mesh, the action of the $e^{-i(\Delta t/2)V}$ operator is local. The action of the $e^{-i\Delta t H_0}$ operator with Hermitian Hamiltonian H_0 is calculated using Lanczos pseudospectral algorithm.[52,58] The Fourier-grid pseudospectral method[59,60] is used to calculate the spatial derivatives entering H_0. We perform a change of variables (mapping[61]) in order to obtain the tight mesh in the vicinity of medium interfaces so that the boundary conditions are accurately reproduced. The calculation mesh typically comprises $256(N_z)\times 64(N_x)\times 64(N_y)$ points and covers the $-9D\le z\le 1D$ region perpendicular to the sample and one period D along the x and y axes. The convergence tests were performed with doubling the number of points in each dimension.

Single time-propagation run allows one to obtain the scattering properties of the system within certain frequency range. To this end, the Gaussian initial wave packet incident on the structure along the z axis is used,

$$\Psi_0=\begin{pmatrix}\hat{\mathbf{e}}_x\\ \hat{\mathbf{e}}_y\\ 0\end{pmatrix}e^{-[(z-z_0)/\Lambda]^2}e^{ik_0 z}, \tag{6}$$

where $\hat{\mathbf{e}}_x$ and $\hat{\mathbf{e}}_y$ are the unit vectors along the x and y axes, correspondingly. The Λ and k_0 parameters are set in such a way that the spectrum of Ψ_0 covers the frequency range of interest. The frequency-resolved reflection coefficients within each diffraction order are obtained via the time-to-frequency Fourier transform of the signal at some distance in front of the structure[62,63] (see Appendix for more details). Besides the far fields (scattering matrix), the near fields can be extracted at desired frequency,

$$\Psi(\omega)=\int_0^\infty e^{i(\omega+i\eta)t}\Psi(t)dt\big|_{\eta\to+0}. \tag{7}$$

In practice, the upper integration limit is given by the finite propagation time. It has to be large enough to converge $\Psi(\omega)$, which might cause some problems when the long-lived states are present in the system.

III. RESULTS AND DISCUSSION

In Figs. 2 and 3 we show the calculated reflectivity spectra of the gold surface with square array of pyramidal pits and compare it with experimental data of Perney *et al.*[46] The calculated specular $\mathcal{R}_{00}$ and total R reflection coefficients are presented as functions of the wavelength λ of the incident radiation. R is obtained from the sum of the outgoing fluxes in all open diffraction channels (see Appendix). Here, the diffraction channel (ℓ,j) associated with exchange of $\ell(j)$ reciprocal-lattice vectors in $x(y)$ direction is open when $\lambda<\lambda_{\ell,j}$, where the threshold wavelength is given by $\lambda_{\ell,j}=D/\sqrt{\ell^2+j^2}$.

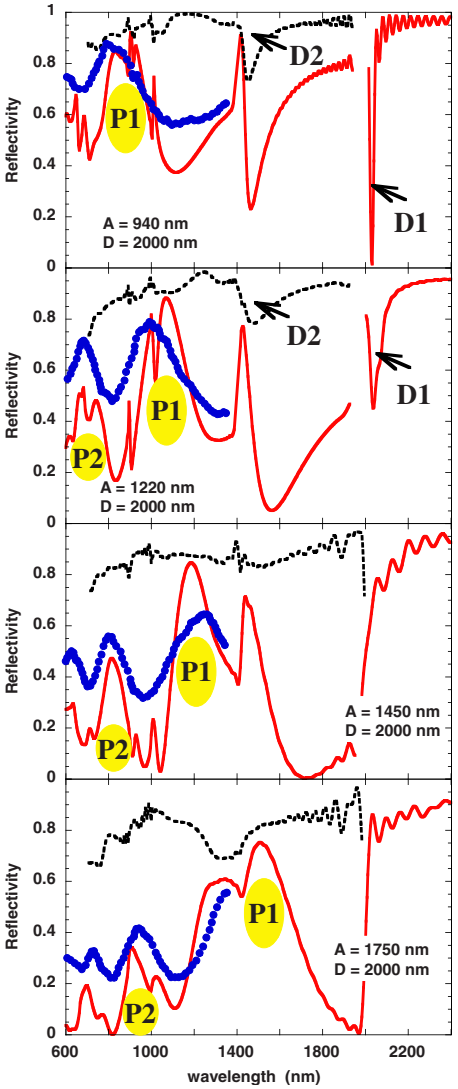

FIG. 2. (Color online) Reflectivity of the metal surface with square array of pyramidal pits. Normal incidence. The results are shown as a function of the wavelength of the incident radiation. Panels of the figure correspond to the arrays characterized by the same period $D=2000$ nm and different pit aperture A as indicated in the insets. Red solid line shows the calculated specular-reflection coefficient $\mathcal{R}_{00}$ and black dashed line shows the calculated total-reflection coefficient R. Experimental data from Ref. 46 is plotted with blue dots. The labeled structures correspond to localized plasmon resonances (P1 and P2) and resonances pinned to the diffraction thresholds (D1 and D2) as discussed in the text.

Following the experimental work, two sets of results are presented. The data in Fig. 2 correspond to the arrays with the same period D but different geometries of the pits given by the aperture A (see Fig. 1). The data in Fig. 3 correspond to the arrays characterized by the same pit geometry but different periods. This way of the data analysis eases the identification of the (i) resonances pinned to the diffraction thresholds and associated with excitation of the surface-plasmon polaritons and (ii) resonances due to the excitation

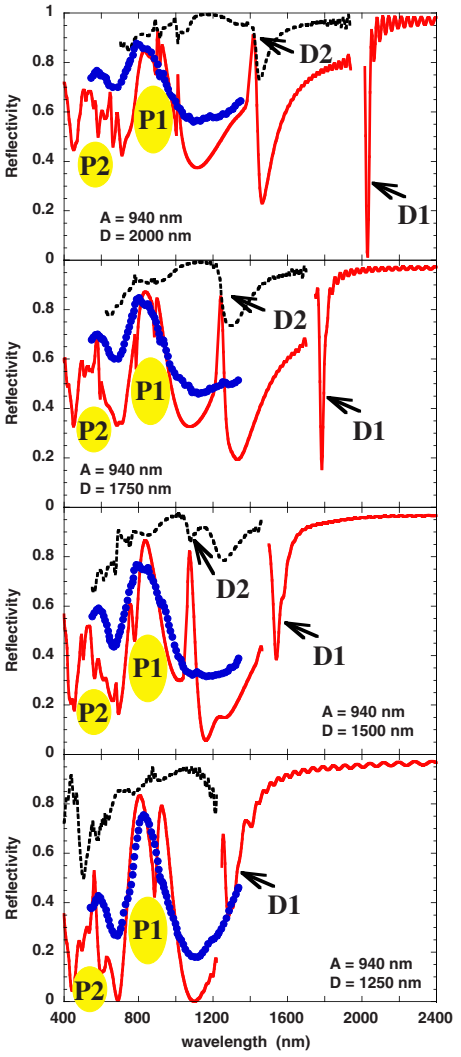

FIG. 3. (Color online) Same as Fig. 2, but for the pyramidal pit arrays characterized by the same pit aperture $A=940$ nm and different periods D as indicated in the insets of each panel.

of the pit-localized plasmons appearing at the frequencies determined by the pit geometry only. In order to reveal the most prominent (i)-type feature associated with first diffraction threshold and to allow a systematic study, the calculations were performed in the wavelength range essentially larger than that of the experiment.

As a first observation, calculated wavelength dependence of the specular-reflection coefficient (zero diffraction order) closely corresponds to the experimental data. In particular, positions of the maxima and minima are nicely reproduced. The quantitative differences arise because the experiment had integrated over certain range of scattering angles and thus some of the diffracted beams were (partly) collected. It is quite remarkable that while the specular-reflection coefficient presents strong variations with wavelength of the incident radiation, the total reflection is much less structured and stays at 0.8–0.9 level. It is mostly affected by the resonances pinned to the diffraction thresholds and associated with excitation of SPPs (see below).

For the normal-incidence case considered here the total-reflection coefficient $R=\mathcal{R}_{00}$ when $\lambda \geq D$ so that we only show $\mathcal{R}_{00}$ at these wavelengths. It is worth noting that WPP method, as many of the time-domain techniques, implies necessity of the time-to-frequency Fourier transform in order to get frequency-resolved data from the calculated time dependence of the fields (see Appendix). Since the solution is known only for finite propagation times, the results are difficult to converge immediately above the first diffraction threshold at $\lambda \lesssim D$. This is because of the sharp threshold behavior, opening of the new diffraction channels and nearby resonance. Therefore, the reflection coefficients are not shown in immediate vicinity of the first diffraction threshold at $\lambda = D - \epsilon$. The oscillations at large wavelength are also linked to the Fourier analysis at finite propagation times. We would like to stress that these computational issues do not concern the results in the interval of the experimental wavelengths as well as the assignment of different structures in the wavelength dependence of reflectivity.

We start our detailed analysis with Fig. 2 corresponding to the fixed structure period $D=2000$ nm. For the pit aperture $A=940$ nm the filling factor is small so that the plasmon-polariton mode propagating on the flat patches of the Au surface is well defined. The resonant features appearing below the diffraction thresholds can then be linked with excitation of SPPs as has been discussed for metallic gratings.[5] Particularly pronounced are the large wavelength resonances D1 and D2 located next to the lowest diffraction thresholds $\lambda_{\pm 1,0}=\lambda_{0,\pm 1}=D$ and $\lambda_{\pm 1,\pm 1}=D/\sqrt{2}$, respectively. The D1 resonance has the smallest width since it decays only via emission of radiation perpendicular to the surface (zero diffraction order) and via energy dissipation in the metal. We will denote the corresponding decay rates as Γ_{rad} and Γ_{diss}. The D2 resonance is essentially broader because its radiative decay involves light emission into the zero and first diffraction orders.

It is remarkable that for $D=2000$ nm and $A=940$ nm the D1 resonance at $\lambda \gtrsim D$ is associated with strong light absorption at corresponding wavelength. According to the general theoretical framework based on the Breit-Wigner formalism in scattering theory,[64] this implies[18,42] $\Gamma_{\mathrm{rad}} \approx \Gamma_{\mathrm{diss}} \approx \Gamma/2$, where $\Gamma=\Gamma_{\mathrm{rad}}+\Gamma_{\mathrm{diss}}$ is the total decay rate. Since Γ_{rad} can be tuned through the choice of the pit aperture A, one can *a priori* reach the situation where $\Gamma_{\mathrm{rad}}=\Gamma_{\mathrm{diss}}=\Gamma/2$ leading to the 100% absorption. Observe that because of the symmetry the effect is polarization independent at normal incidence so that the present system can be as efficient absorber as metallic-grating structures.[16,17,20,65] The D2 resonance at $\lambda \gtrsim D/\sqrt{2}$ is associated with much less absorption consistent with its large radiative decay rate.

When the aperture of the pitch A increases, the D1 and D2 resonances broaden and basically disappear for $A=1450$ nm. Indeed, the filling factor is large and the surface is strongly corrugated. As a result (i) the resonances are strongly coupled with radiation continua and quickly decay and (ii) the flat patches of the surface are nearly vanishing so they are unable to host the SPPs. The opening of diffraction channels with decreasing wavelength still leads to the prominent features in the specular reflection, however the total-reflection coefficient stays rather flat.

As an interesting effect, we obtain that for $A/D \sim 0.75$ [Fig. 2 (third panel) and Fig. 3 (fourth panel)] the specular

reflection is completely suppressed for the wavelengths $\lambda \approx 0.85D$, i.e., between the first and second diffraction thresholds. Provided the total reflection coefficient at 0.8 level, this implies that all the scattered flux is diverged into the nonspecular (diffracted) beams associated with one reciprocal-lattice-vector exchange with the structure.

In certain wavelength intervals, the features in specular-reflection coefficient linked with diffraction thresholds and excitation of the propagating SPPs are superimposed on the broad resonant structures labeled P1 and P2. These resonances lead to strong enhancement of the specular reflection. Diffracted beams are suppressed particularly for the lower-frequency P1 resonance. While the specular reflection is strongly affected, the total reflection coefficient varies only mildly through the resonance so that the latter is not associated with enhanced absorption, in contrast to, e.g., D1 resonance pinned to the lowest diffraction threshold. This can be understood with help of the following argument: the enhanced absorption requires a large enough lifetime of the trapped mode so that the electromagnetic field stays for sufficient time in contact with metal to induce appreciable energy transfer to the electronic excitations. In terms of the decay rates introduced above one needs $\Gamma_{\mathrm{rad}} \sim \Gamma_{\mathrm{diss}}$.[18,42,66] This is apparently not the case for the present resonant structures characterized by the large Γ_{rad} as can be inferred from their widths. Thus, no efficient absorption occurs. Based on the analysis presented below we ascribe these resonant features to the excitation of the pit-localized plasmons.

The first argument in favor of the pit-localized nature of the trapped modes associated with P1 and P2 resonances comes from the results presented in Fig. 3. The reflectivity spectra are shown for the pyramidal pit arrays with various periods D but the same pit aperture $A=940$ nm. All the diffraction structures as well as the D1 and D2 resonances pinned to diffraction thresholds shift to smaller wavelength with decreasing period. At variance, the P1 and P2 resonances remain at the same position *independent of the period of the structure and dependent on the geometry of the pits only*. Indeed, it follows from Figs. 2 and 3 that P1 and P2 shift to higher wavelength with increasing size of the pyramidal pits A. Therefore, one can infer that the corresponding trapped fields should be localized inside the pits so that the neighbor pits hardly interact, similar to the case of the plasmons localized in spherical voids.[30,33,34]

The unambiguous assignment of the resonant structures in the reflectivity spectra and the final proof of the pit-localized plasmon origin of the P1 and P2 resonances come from the analysis of the frequency-resolved near fields. In Fig. 4 we show the field intensity I defined as $I=|E_x|^2+|E_y|^2+|E_z|^2$ for the pit arrays characterized by the same period $D=2000$ nm and different sizes of the pit aperture A. The results are represented in the (x,z) plane as defined in Fig. 1. The near fields are extracted from the WPP at the wavelengths listed in Table I and correspond to the D1, D2, P1, and P2 structures in Fig. 2. (In Fig. 4 we keep the same notations.) Thus, combining the reflectivity spectra and the near-field analysis one obtains a rather complete description of the system. Two distinctly different types of the near fields are observed.

(1) The near fields corresponding to the resonances D1 and D2 pinned to the diffraction thresholds and associated

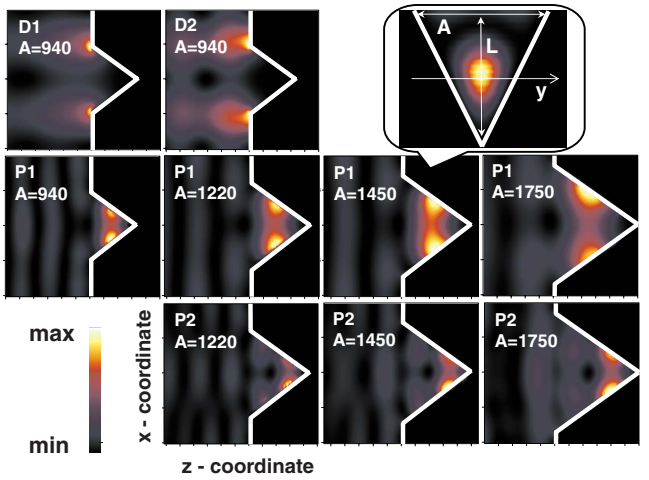

FIG. 4. (Color online) Intensity of the electromagnetic field $I=|E_x|^2+|E_y|^2+|E_z|^2$ as a function of the z and x coordinates. Results are presented in the (x,z) plane perpendicular to the surface and containing the apex of the pit (see Fig. 1 for definition of the coordinate system). The metal surface is shown with white line. Different panels show the results obtained for the pit arrays characterized by the same period $D=2000$ nm and pit aperture A indicated in the insets (in nm). The fields are extracted from the WPP calculations at the wavelengths corresponding to the diffraction (D1 and D2) and pit-localized plasmon (P1 and P2) resonances indicated in Fig. 2. The framed inset shows the intensity of the field of the P1 resonance in immediate vicinity of the metal face of the pit with $A=1450$ nm. L is a bisector of the pyramidal face.

with excitation of the SPPs look very much the same for all pit apertures A. We then only show them for $A=940$ nm. Exception is the $A=1750$ nm case, where the surface gets extremely corrugated with very small flat patches thus D1 and D2 resonances basically disappear, as discussed earlier. As follows from our results, the trapped modes underlying the D1 and D2 resonances are characterized by very strong field enhancements at the ridge between the flat patch of the surface and the pyramidal pit. Quite similar results have been reported for different types of the periodic cavity arrangements at the surface, in particular for the arrays of square and rectangular holes.[67–69]

(2) The extracted near fields corresponding to the P1 and P2 resonances fully confirm an assignment of the broad

TABLE I. The wavelength λ at which the near fields shown in Fig. 4 have been extracted from the time-dependent solution of Maxwell's equations. The extraction has been done for the pit arrays with the same period $D=2000$ nm but different pit aperture sizes A. Notation of the resonances corresponds to the one used in Figs. 2–4.

Resonance	Aperture A (nm)	Wavelength λ (nm)
D1, D2	940	2030, 1418
P1	940	828
P1, P2	1220	1068, 741
P1, P2	1450	1309, 820
P1, P2	1750	1508, 950

peaks in the specular-reflection coefficient as due to the excitation of pit-localized plasmons. The electric field of the trapped modes is well confined inside the pyramidal pit and the overall shape of the field does not depend on the pit aperture A. For the lowest frequency mode P1, the maximum field intensity is reached close to the metal surface of the opposite pit faces parallel to the y axis. The field is zero (not shown in the figure) at another two pit faces parallel to x axis as can be understood as a consequence of the polarization of the incident electromagnetic wave. The second higher-frequency mode P2 shows two maxima along the pit face. The P2 mode is not presented for the smallest aperture size $A=940$ nm since corresponding frequency is too high and appears out of the calculation range. The fact that the resonant fields are buried below the surface plane naturally explains the enhancement of the specular reflection at resonance. Indeed, pit-localized resonances mainly decay via radiation in the direction perpendicular to the surface. The radiation in grazing directions is prevented by the surrounding metal.

Following ideas proposed in Refs. 45 and 46, the results can be understood as confinement of the plasmon polariton propagating along the metal face of the pyramid. The resonator character of the pit is reflected by the nodal structure of the field intensity at the pit sidewall. Here, the node at the intersection between pyramidal pit and metal surface indicates partial decoupling of the localized mode from the radiation continuum. The difference between the present 3D case and the 2D case of a V-shaped groove used to model the experimental data in Ref. 45 consists of the boundary conditions imposed by the pit sidewalls next to those hosting the localized plasmon. The field components perpendicular to the surface of the given face of the pit appear parallel to the surface of the neighbor faces. This results in a zero boundary conditions on the field at the edges of the pit, as nicely seen in the inset of Fig. 4 showing the field intensity of the lowest-frequency P1 resonance in the vicinity of the metal face of the inverted pyramid. Because of the boundary conditions the field is expelled from the apex of the 3D pyramidal pit. We recall that field maximum has been reported at the bottom of the 2D V-shaped groove.[45]

With account for the above boundary conditions one can estimate the wavelengths of the incident radiation resonant with pit-localized plasmons. Consistent with localized character of the field, the interaction between neighboring pits, i.e., the dependence on the period of the structure, is neglected. Consider the lowest-frequency-plasmon mode P1 localized at the middle of the triangular pit sidewall as shown in the inset of Fig. 4. We define two perpendicular directions: L direction along the bisector of pyramidal face given by the cut of the pit sidewall by the (x,z) plane and y direction parallel to the y axis. In a very crude approximation, the zero boundary conditions at the edges of the pit imply the quantization of the surface-plasmon-wave vector along the corresponding directions,

$$k_L = \pi/L = \frac{2\pi}{A}\sin(\alpha/2), \quad k_y = \frac{2\pi}{A}. \tag{8}$$

The total wave vector of the plasmon is given by

TABLE II. Estimated wavelength of the incident radiation resonant with the pit-localized plasmons. The λ_{P1} [Eq. (10)] and λ_{P2} [Eq. (11)] are tabulated for different pit apertures A.

A (nm)	λ_{P1} (nm)	λ_{P2} (nm)
940	814	543
1220	1056	704
1450	1255	837
1750	1515	1010

$$k = \frac{2\pi}{A}\sqrt{1+\sin^2(\alpha/2)}. \tag{9}$$

Within the frequency range considered here the surface-plasmon dispersion closely follows the light line so that the wavelength of the incident radiation resonant with lowest energy pit-localized plasmon mode is then given by

$$\lambda_{P1} = A/\sqrt{1+\sin^2(\alpha/2)}. \tag{10}$$

The situation with the second P2 (higher frequency) plasmon resonance is more intricate. As follows from our numerical results, the first maximum of the field is located not at $L/4$ as one would expect for the perfect resonator but rather at $L/3$. We tentatively attribute this effect to the fact that the closer the first maximum is to the pit apex the higher will be the frequency of the corresponding mode because of the zero boundary conditions at the edges (y direction). Thus, the system lowers its energy extending into the vacuum side above the surface so that the first maximum shifts further away from the pit apex. If we use numerically calculated value of $L/3$ to define the k_L and k_y wave vectors, we obtain the following resonance wavelength:

$$\lambda_{P2} = 2A/3\sqrt{1+\sin^2(\alpha/2)} = 2\lambda_{P1}/3. \tag{11}$$

The λ_{P1} and λ_{P2} wavelengths obtained from Eqs. (10) and (11) are listed in Table II for the pit arrays characterized by different apertures size A. Provided simplicity of the above model, the agreement between the estimated resonance wavelengths and positions of the maxima in the calculated specular-reflection coefficient (Figs. 2 and 3) is remarkable.

Finally, in order to complete the characterization of the pit-localized plasmons, the E_z component of the near fields of the P1 and P2 resonances is shown in Fig. 5. Results are presented for the pyramidal pit array characterized by $D=2000$ nm and $A=1450$ nm. One observes the dipolar character of the lower-frequency P1 resonance with opposite signs of the fields at the opposite faces of the pit. The second resonance P2 shows a quadrupole character with the field sign change not only at the opposite faces but also along the same face. Consistent with normal incidence and polarization of incoming light along the x axis, the states are antisymmetric with respect to the (y,z) plane going through the apex of the pyramid.

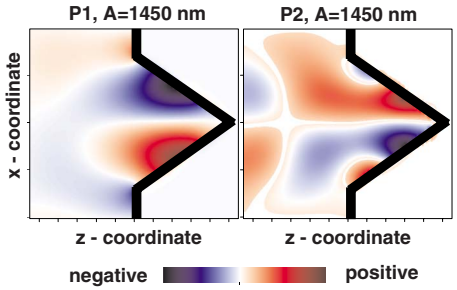

FIG. 5. (Color online) E_z component of the near field corresponding to the excitation of the pit-localized plasmons P1 and P2 for the pyramidal pit array characterized by $D=2000$ nm and aperture size $A=1450$ nm. Results are presented as a function of the z and x coordinates in the (x,z) plane perpendicular to the surface and containing the apex of the pit (see Fig. 1 for definition of the coordinate system).

IV. SUMMARY AND CONCLUSIONS

We have performed the rigorous calculation of the electromagnetic reflection spectra for the gold substrate composed of square periodic array of inverted pyramidal pits. The case of the normal incidence has been considered. Our 3D numerical study is based on the time-domain wave-packet propagation approach.[52] The main ingredients of the method are (i) the Hamiltonian formalism for evolution operator, (ii) the Lanczos time-propagation scheme, and (iii) the mapped Fourier-grid pseudospectral method so that the spatial grid resolution is enhanced at material interfaces.

Present theoretical results are in a good agreement with recently published experimental data.[46] This validates the methods employed and allows unambiguous assignment of the resonance structures in the reflection spectra.

We show that, similar to the metal surfaces with spherical voids,[30–35] the gold surface with inverted pyramidal pits supports both (i) the delocalized surface-plasmon-polariton modes leading to the prominent resonant structures pinned to the diffraction thresholds and (ii) pit-localized plasmons with frequencies determined by the geometry of pyramidal pits and independent of the structure period.

Similar to metallic gratings, the resonant features at diffraction thresholds are associated with enhanced absorption of the incident radiation. For some combinations of the structure period D and pit aperture A nearly complete polarization-independent absorption can be reached for normal incidence at lower-frequency resonance. At variance, the radiative decay of the pit-localized plasmons is too fast to have appreciable energy transfer to the substrate and so notable absorption. The pit-localized plasmons reveal themselves through the resonant enhancement of the specular reflection at nearly constant total-reflection coefficient.

For the pit-localized plasmons, the near-field analysis shows the field enhancement inside the pit and close to the opposite metal faces of the pyramid. In the case of the resonances at diffraction thresholds, the fields are strongly enhanced at the ridges between the flat patch of the surface and the pyramidal pit.

Since the resonance frequencies are controlled by the geometrical parameters of the structure, the latter can be considered as possible tunable substrate for the surface-enhanced Raman scattering. In this perspective, with proper choice of the boundary conditions explained in the paper, the wavelength of the incident radiation resonant with pit-localized plasmons can be estimated from simple model describing the pit-localized plasmons as due to the confinement of the plasmon polariton propagating along the metal face of the pyramid.

Finally, it is worth mentioning that besides different (localized and delocalized) plasmon modes and aforementioned polarization-independent strong absorption at normal incidence, present nanostructured surface shows another interesting feature. Namely, at certain wavelengths and for the certain geometries we observe complete suppression of specular reflection. The scattered intensity is transferred into nonspecular diffracted beams.

ACKNOWLEDGMENTS

Many fruitful discussions with J. P. Gauyacq are gratefully acknowledged. We gratefully acknowledge J. J. Baumberg for the kind permission to use his original artwork for Fig. 1 of the present paper.

APPENDIX

In this appendix we describe the "virtual detector" approach[62,63] used here to extract the reflection properties within a broad frequency range from a single wave-packet-propagation run.

As described in the main text we use the initial state for the time propagation as a Gaussian wave packet localized at $z<z_*$ region and incident at the structure.

The electric field $\mathbf{E}(\mathbf{r},t)$ in the asymptotic region above the metal surface is given by the superposition of the corresponding Fourier modes,

$$\mathbf{E}(\mathbf{r},t)=\sum_{\ell,j} e^{iG(\ell x+jy)}\int_{-\infty}^{+\infty} d\omega e^{-i\omega t} \times[\mathbf{E}^{+}_{\ell j}(\omega)e^{ik_{\ell j}z}+\mathbf{E}^{-}_{\ell j}(\omega)e^{-ik_{\ell j}z}], \quad \text{(A1)}$$

where the pair of integers (ℓ,j) denotes the diffraction (scattering) channel and $G=2\pi/D$ is the elementary vector of the reciprocal lattice. Here we take into account that the structure under study is a square periodic array in x and y directions. The wave vector in z direction $k_{\ell j}$ is given by

$$k_{\ell j}=\sqrt{\omega^2/c^2-G^2(\ell^2+j^2)}. \quad \text{(A2)}$$

The integration and summation in Eq. (A1) runs only over the propagating fields in open diffraction channels. $\mathbf{E}^{\pm}_{\ell j}(\omega)=0$ if $\omega^2-c^2G(\ell^2+j^2)<0$ (closed diffraction channels).

We are interested in finding the amplitudes $\mathbf{E}^{\pm}_{\ell j}$. Then, for a fixed z_1 and z_2 located between the metal surface and initial wave packet we first extract the time-dependent projections,

$$\mathbf{F}^{1,2}_{nm}(t)=\int_0^D\int_0^D \frac{dxdy}{D^2} e^{-iG(nx+my)}\mathbf{E}(x,y,z_{1,2},t). \quad \text{(A3)}$$

It follows from Eq. (A1) that

$$\mathbf{F}_{nm}^{1,2}(t) = \int_{-\infty}^{+\infty} d\omega e^{-i\omega t}[\mathbf{E}_{nm}^{+}(\omega)e^{ik_{nm}z_{1,2}} + \mathbf{E}_{nm}^{-}(\omega)e^{-ik_{nm}z_{1,2}}]. \tag{A4}$$

$\mathbf{F}_{nm}^{1,2}(t)$ can be viewed as a signal measured by the virtual detectors positioned at z_1 and z_2. By carrying out the Fourier transform of the signal at positive frequency $\Omega > 0$, we find

$$\mathbf{G}_{nm}^{1,2}(\Omega) = \frac{1}{2\pi}\int_{-\infty}^{+\infty} dt e^{i\Omega t}\mathbf{F}_{nm}^{1,2}(t) = \mathbf{E}_{nm}^{+}(\Omega)e^{ik_{nm}z_{1,2}} + \mathbf{E}_{nm}^{-}(\Omega)e^{-ik_{nm}z_{1,2}}. \tag{A5}$$

The amplitudes $\mathbf{E}_{nm}^{\pm}(\Omega)$ can now be obtained from $\mathbf{G}_{nm}^{1}(\Omega)$ and $\mathbf{G}_{nm}^{2}(\Omega)$ by solving a system of two linear equations. For $\Omega > 0$ the $\mathbf{E}_{nm}^{+}(\Omega)$ is the amplitude of the incident wave and $\mathbf{E}_{nm}^{-}(\Omega)$ is the amplitude of the scattered wave.

Two important remarks are in order. First, the numerical solution of Maxwell's equations is known only for a positive propagation time $t > 0$. However, since the detectors are placed between the incident wave packet and the surface, it follows from the causality that $\mathbf{F}_{nm}^{1,2}(z,t) = 0$ for $t < 0$. So the numerical integration in Eq. (A5) can be started at $t = 0$. Second, the upper integration limit in Eq. (A5) is fixed by the total numerical propagation time T. It must be large enough to ensure a desired accuracy. In particular, if a photonic structure has resonances, one might need very large T to ensure the convergence.

The incoming (+) or outgoing (−) flux in each (ℓ, j) scattering channel is given by the Poynting vector,

$$\mathbf{S}_{\ell j}^{\pm} = \frac{c}{4\pi}\mathbf{E}_{\ell j}^{\pm} \times \mathbf{B}_{\ell j}^{\pm} = \frac{c}{4\pi}\sqrt{\epsilon}\frac{\mathbf{k}}{k}|\mathbf{E}_{\ell j}^{\pm}|^2. \tag{A6}$$

The flux component in the direction normal to the structure is

$$\hat{\mathbf{e}}_z \cdot \mathbf{S}_{\ell j}^{\pm}(\Omega) = \pm \frac{c^2}{4\pi}\frac{k_{\ell j}}{\Omega}|\mathbf{E}_{\ell j}^{\pm}(\Omega)|^2. \tag{A7}$$

In the present work the incident wave packet is chosen to contain only the $(\ell = 0, j = 0)$ waves (normal incidence). Using Eq. (A7) the corresponding reflection coefficient into the given diffraction channel is given by the ratio between outgoing and incident fluxes,

$$\mathcal{R}_{\ell j}(\Omega) = \left|\frac{\hat{e}_z \mathbf{S}_{\ell j}^{-}(\Omega)}{\hat{e}_z \mathbf{S}_{00}^{+}(\Omega)}\right|. \tag{A8}$$

$\mathcal{R}_{00}(\Omega)$ is the specular-reflection coefficient. Obviously, $R(\Omega) = \Sigma_{\ell j}\mathcal{R}_{\ell j}(\Omega)$ gives the total reflection coefficient. (The summation runs only over open diffraction channels.)

It is worth mentioning that in some cases only one detector is sufficient. From the causality the amplitudes $\mathbf{E}_{\ell j}^{+}(\Omega)$ are nonzero only for the incident channel. Therefore, for all other channels the amplitudes $\mathbf{E}_{\ell j}^{-}(\Omega)$ can be extracted with a single detector.

*Corresponding author; tatiana.teperik@institutoptique.fr

[1] A. V. Zayats, I. I. Smolyaninov, and A. A. Maradudin, Phys. Rep. **408**, 131 (2005).
[2] F. J. García de Abajo, Rev. Mod. Phys. **79**, 1267 (2007).
[3] C. Genet and T. W. Ebbesen, Nature (London) **445**, 39 (2007).
[4] T. W. Ebbesen, H. J. Lezec, H. F. Ghaemi, T. Thiol, and P. A. Wolff, Nature (London) **391**, 667 (1998).
[5] J. A. Porto, F. J. García-Vidal, and J. B. Pendry, Phys. Rev. Lett. **83**, 2845 (1999).
[6] M. M. J. Treacy, Phys. Rev. B **66**, 195105 (2002).
[7] F. Yang and J. R. Sambles, Phys. Rev. Lett. **89**, 063901 (2002).
[8] S. A. Darmanyan and A. V. Zayats, Phys. Rev. B **67**, 035424 (2003).
[9] F. J. García de Abajo and J. J. Sáenz, Phys. Rev. Lett. **95**, 233901 (2005).
[10] D. Pacifici, H. J. Lezec, L. A. Sweatlock, R. J. Walters, and H. A. Atwater, Opt. Express **16**, 9222 (2008).
[11] H. Liu and P. Lalanne, Nature (London) **452**, 728 (2008).
[12] U. Schröter and D. Heitmann, Phys. Rev. B **58**, 15419 (1998).
[13] H. E. Went, A. P. Hibbins, J. R. Sambles, C. R. Lawrence, and A. P. Crick, Appl. Phys. Lett. **77**, 2789 (2000).
[14] Q. Cao and P. Lalanne, Phys. Rev. Lett. **88**, 057403 (2002).
[15] F. Marquier, J.-J. Greffet, S. Collin, F. Pardo, and J. L. Pelouard, Opt. Express **13**, 70 (2005).
[16] M. C. Hutley and D. Maystre, Opt. Commun. **19**, 431 (1976).
[17] E. Popov, L. Tsonev, and D. Maystre, Appl. Opt. **33**, 5214 (1994).
[18] W. C. Tan, J. R. Sambles, and T. W. Preist, Phys. Rev. B **61**, 13177 (2000).
[19] S. Collin, F. Pardo, R. Teissier, and J. L. Pelouard, Appl. Phys. Lett. **85**, 194 (2004).
[20] N. Bonod, G. Tayeb, D. Maystre, S. Enoch, and E. Popov, Opt. Express **16**, 15431 (2008).
[21] M. Laroche, C. Arnold, F. Marquier, R. Carminati, J. J. Greffet, S. Collin, N. Bardou, and J. L. Pelouard, Opt. Lett. **30**, 2623 (2005).
[22] Y. De Wilde, F. Formanek, R. Carminati, B. Gralak, P.-A. Lemoine, K. Joulain, J.-P. Mulet, Y. Chen, and J.-J. Greffet, Nature (London) **444**, 740 (2006).
[23] G. Biener, N. Dahan, A. Niv, V. Kleiner, and E. Hasmana, Appl. Phys. Lett. **92**, 081913 (2008).
[24] J. Le Perchec, P. Quémerais, A. Barbara, and T. López-Ríos, Phys. Rev. Lett. **100**, 066408 (2008).
[25] C. Girard, Rep. Prog. Phys. **68**, 1883 (2005).
[26] S. I. Bozhevolnyi, V. S. Volkov, E. Devaux, J.-Y. Laluet, and T. W. Ebbesen, Nature (London) **440**, 508 (2006).
[27] L. Aigouy, P. Lalanne, J. P. Hugonin, G. Julié, V. Mathet, and M. Mortier, Phys. Rev. Lett. **98**, 153902 (2007).
[28] J.-C. Weeber, A. Bouhelier, G. Colas des Francs, L. Markey, and A. Dereux, Nano Lett. **7**, 1352 (2007).
[29] V. Mikhailov, G. A. Wurtz, J. Elliott, P. Bayvel, and A. V. Zayats, Phys. Rev. Lett. **99**, 083901 (2007).
[30] S. Coyle, M. C. Netti, J. J. Baumberg, M. A. Ghanem, P. R. Birkin, P. N. Bartlett, and D. M. Whittaker, Phys. Rev. Lett. **87**,

176801 (2001).
[31] P. N. Bartlett, J. J. Baumberg, S. Coyle, and M. Abdelsalem, Faraday Discuss. **125**, 117 (2004).
[32] S. Coyle, G. V. Prakash, J. J. Baumberg, M. Abdelsalem, and P. N. Bartlett, Appl. Phys. Lett. **83**, 767 (2003).
[33] T. V. Teperik, V. V. Popov, F. J. García de Abajo, M. Abdelsalam, P. N. Bartlett, T. A. Kelf, Y. Sugawara, and J. J. Baumberg, Opt. Express **14**, 1965 (2006).
[34] T. V. Teperik, V. V. Popov, F. J. García de Abajo, T. A. Kelf, Y. Sugawara, J. J. Baumberg, M. Abdelsalam, and P. N. Bartlett, Opt. Express **14**, 11964 (2006).
[35] R. M. Cole, J. J. Baumberg, F. J. García de Abajo, S. Mahajan, M. Abdelsalam, and P. N. Bartlett, Nano Lett. **7**, 2094 (2007).
[36] A. Christ, T. Zentgraf, J. Kuhl, S. G. Tikhodeev, N. A. Gippius, and H. Giessen, Phys. Rev. B **70**, 125113 (2004).
[37] A. Christ, S. G. Tikhodeev, N. A. Gippius, J. Kuhl, and H. Giessen, Phys. Rev. Lett. **91**, 183901 (2003).
[38] C. Ropers, D. J. Park, G. Stibenz, G. Steinmeyer, J. Kim, D. S. Kim, and C. Lienau, Phys. Rev. Lett. **94**, 113901 (2005).
[39] V. G. Kravets, F. Schedin, and A. N. Grigorenko, Phys. Rev. Lett. **101**, 087403 (2008).
[40] B. Auguié and W. L. Barnes, Phys. Rev. Lett. **101**, 143902 (2008).
[41] T. V. Teperik, V. V. Popov, and F. J. García de Abajo, J. Opt. A, Pure Appl. Opt. **9**, S458 (2007).
[42] T. V. Teperik, F. J. García de Abajo, A. G. Borisov, M. Abdelsalam, P. N. Bartlett, Y. Sugawara, and J. J. Baumberg, Nat. Photonics **2**, 299 (2008).
[43] B. Pettinger, G. Picardi, R. Schuster, and G. Ertl, Single Mol. **3**, 285 (2002).
[44] S. Mahajan, J. J. Baumberg, A. E. Russell, and P. N. Bartlett, Phys. Chem. Chem. Phys. **9**, 6016 (2007).
[45] N. M. B. Perney, J. J. Baumberg, M. E. Zoorob, M. D. B. Charlton, S. Mahnkopf, and M. C. Netti, Opt. Express **14**, 847 (2006).
[46] N. M. B. Perney, F. J. García de Abajo, J. J. Baumberg, A. Tang, M. C. Netti, M. D. B. Charlton, and M. E. Zoorob, Phys. Rev. B **76**, 035426 (2007).
[47] J. R. Krenn, A. Dereux, J. C. Weeber, E. Bourillot, Y. Lacroute, J. P. Goudonnet, G. Schider, W. Gotschy, A. Leitner, F. R. Aussenegg, and C. Girard, Phys. Rev. Lett. **82**, 2590 (1999).
[48] K. Li, M. I. Stockman, and D. J. Bergman, Phys. Rev. Lett. **91**, 227402 (2003).
[49] C. E. Talley, J. B. Jackson, C. Oubre, N. K. Grady, C. W. Hollars, S. M. Lane, T. R. Huser, P. Nordlander, and N. J. Halas, Nano Lett. **5**, 1569 (2005).
[50] F. Hao, C. L. Nehl, J. H. Hafner, and P. Nordlander, Nano Lett. **7**, 729 (2007).
[51] M. Pelton, J. Aizpurua, and G. W. Bryant, Laser Photonics Rev. **2**, 136 (2008).
[52] A. G. Borisov and S. V. Shabanov, J. Comput. Phys. **209**, 643 (2005).
[53] A. G. Borisov and S. V. Shabanov, J. Comput. Phys. **199**, 742 (2004).
[54] M. Kreiter, S. Mittler, W. Knoll, and J. R. Sambles, Phys. Rev. B **65**, 125415 (2002).
[55] D. Neuhauser and M. Baer, J. Chem. Phys. **91**, 4651 (1989).
[56] T. Seideman and W. H. Miller, J. Chem. Phys. **97**, 2499 (1992).
[57] M. D. Feit, J. A. Fleck, Jr., and A. Steiger, J. Comput. Phys. **47**, 412 (1982).
[58] For quantum-mechanical time-domain techniques see review paper by C. Leforestier, R. H. Bisseling, C. Cerjan, M. D. Feit, R. Friesner, A. Guldberg, A. Hammerich, G. Jolicard, W. Karrlein, H. D. Meyer, N. Lipkin, O. Roncero, and R. Kosloff, J. Comput. Phys. **94**, 59 (1991).
[59] R. Kosloff, J. Phys. Chem. **92**, 2087 (1988).
[60] C. C. Marston and G. G. Balint-Kurti, J. Chem. Phys. **91**, 3571 (1989).
[61] E. Fattal, R. Baer, and R. Kosloff, Phys. Rev. E **53**, 1217 (1996).
[62] A. J. H. M. Meijer, E. M. Goldfield, S. K. Gray, and G. G. Balint-Kurti, Chem. Phys. Lett. **293**, 270 (1998).
[63] J. Sjakste, A. G. Borisov, J. P. Gauyacq, and A. K. Kazansky, J. Phys. B **37**, 1593 (2004).
[64] L. D. Landau and E. M. Lifshitz, *Quantum Mechanics: Non-Relativistic Theory* (Pergamon, Oxford, 1981).
[65] G. H. Derrick, R. C. McPhedran, D. Maystre, and M. Neviere, Appl. Phys. (Berlin) **18**, 39 (1979).
[66] T. V. Teperik, V. V. Popov, and F. J. García de Abajo, Phys. Rev. B **71**, 085408 (2005).
[67] S. Selcuk, K. Woo, D. B. Tanner, A. F. Hebard, A. G. Borisov, and S. V. Shabanov, Phys. Rev. Lett. **97**, 067403 (2006).
[68] A. Mary, Sergio G. Rodrigo, L. Martín-Moreno, and F. J. García-Vidal, Phys. Rev. B **76**, 195414 (2007).
[69] C. Sauvan, C. Billaudeau, S. Collin, N. Bardou, F. Pardo, J.-L. Pelouard, and P. Lalanne, Appl. Phys. Lett. **92**, 011125 (2008).